Monitoring and Predicting Desert Locust Plague Severity in Asia–Africa Using Multisource Remote Sensing Time-Series Data

Zhenfeng Shao, Xiaoxiao Feng, Linze Bai, Haiming Jiao, Ya Zhang, Deren Li, Haisheng Fan, Xiao Huang, Yuqi Ding, Orhan Altan, and Nayyer Saleem

***Abstract*—The outbreak of large-scale desert locust plague in 2020 has attracted wide attention in the world and caused serious damage to food security and livelihood of African and Asian people. Remote sensing techniques can provide indirect feedback on locust plagues, facilitating quick, and real-time monitoring of the occurrence and development of locusts, which is of great significance for ensuring national and regional food security and stability. The hidden Markov model (HMM) is a classic machine learning model that has been widely applied in the fields of time-series data mining. In this study, we aim to predict the severity of locust plague in croplands using the time-series dynamic change features extracted from remote sensing data via HMM. In addition, we assess the damages on the croplands using change detection methods by comparing the crop spectrum before and after the locust plague from two-phase (Feburary 23 and March 7, 2020) hyperspectral images covering substudy area (northern Narok, Kenya). Evaluated by the ground truth data, the OA of predicted results of the plague severity in April, May, June, and July are 0.78, 0.71, 0.74, and 0.72, respectively. The land cover classification OA of the substudy area of the two-phase images are 97.45 and 96.14. Our study demonstrates the validity of the HMM-based method using the remote sensing time-series data to predict locust plague and evaluate its damage. The results of the cropland change detection suggest that the damage of locusts can be quantitatively evaluated using hyperspectral images.**

***Index Terms*—Change detection, Hidden Markov Model (HMM), hyperspectral imagery, locust plague prediction, moderate-resolution imaging spectroradiometer (MODIS), semisupervised classification.**

Manuscript received May 31, 2021; revised July 22, 2021 and August 10, 2021; accepted August 11, 2021. Date of publication August 16, 2021; date of current version September 9, 2021. This work was supported in part by the National Key Research and Development Program of China under Grant 2018YFB0505401, in part by the National Natural Science Foundation of China under Grants 42090012, 41771452, 41771454, and 41901340, and in part by the National Major Project on High Resolution Earth Observation System under Grant GFZX0403260306. *(Corresponding author: Zhenfeng Shao.)*

Zhenfeng Shao, Xiaoxiao Feng, Linze Bai, Haiming Jiao, Ya Zhang, and Deren Li are with the State Key Laboratory of Information Engineering in Surveying, Mapping and Remote Sensing, Wuhan University, Wuhan 430072, China (e-mail: shaozhenfeng@whu.edu.cn; fengxxalice2018@gmail.com; linzebai@whu.edu.cn; 329970350@qq.com; zhangya_rs@whu.edu.cn; drli@whu.edu.cn).

Haisheng Fan is with the The Zhuhai Orbita Aerospace Sciences and Technology Company, Ltd., Zhuhai 519080, China (e-mail: fanhs@casc.ac.cn).

Xiao Huang is with the Department of Geosciences, University of Arkansas, Fayetteville, AR 72701 USA (e-mail: xh010@uark.edu).

Yuqi Ding is with the Department of Computer Science, Louisiana State University, Baton Rouge, LA 70803 USA (e-mail: yding18@lsu.edu).

Orhan Altan is with the Department of Geomatics, Istanbul Technical University, Istanbul 34467, Turkey (e-mail: oaltan@itu.edu.tr).

Nayyer Saleem is with the Survey of Pakistan, Rawalpindi 46000, Pakistan (e-mail: saleemnayyer@whu.edu.cn).

Digital Object Identifier 10.1109/JSTARS.2021.3104936

I. Introduction

IN JUNE 2019, a large-scale locust plague occurred in East Africa and gradually spread to West and South Asia. It has attracted global attention because of its extensiveness, strong destructiveness, and treats many food-producing areas. The outbreak of the locust plague has caused severe damage to parts of Africa–Asia, resulting in crop reduction and serious damage to forestry and grassland natural resources. The Food and Agriculture Organization of the United Nations (FAO) stated that the locust plague posed an unprecedented threat to food security and livelihoods in the Horn of Africa. On February 11, 2020, FAO issued an early warning to the world, as the locust plague has spread to India and Pakistan. Remote sensing-based methods can monitor the occurrence and development of locusts in a timely and comprehensive manner by analyzing the spatiotemporal characteristics of locust plagues with the changes in vegetation, providing references and suggestions, and assisting relevant departments in preventing future locust plagues [1].

Traditional locust monitoring focuses on collecting locust types, numbers, dynamic changes, and other related information through direct or indirect methods. The prediction of locusts is largely based on the collected historical records, which detail locust's habitats, as well as the relevant dynamic monitoring results via applicable mathematical models combined with expert experience. With the development of remote sensing technology [2], [3], the use of satellites for large-scale and real-time monitoring of the occurrence of locust plagues is expected to greatly reduce the costs of locust plague monitoring. Meanwhile, by processing and analyzing these rich satellite data, researchers can extract information on the spatiotemporal variations of locust plagues, providing support for prevention, and prediction. Remote sensing images can be derived from a variety of platforms, including Moderate-Resolution Imaging Spectroradiometer (MODIS), National Oceanic and Atmospheric Administration Advanced Very High-Resolution Radiometer (NOAA AVHRR), and Landsat, to list a few. Sivanpillai *et al.* used imagery from Landsat Enhanced Thematic Mapper (ETM+) to identify locust habitats, providing essential knowledge on locust habitats that benefit pest managers [4]. In the 1980s, [5] predicted the possible occurrence

of locust plagues in Australia based on changes in habitat greenness detected from Landsat Multispectral Scanner (MSS) images. Gomez *et al.* [6] assessed the possibility of using data from the Soil Moisture Active Passive satellite to identify desert locust breeding sites by establishing machine learning models in 31 countries. Their method linked the presence of desert locusts with remotely sensed soil moisture. Vegetation condition is one of the most important indicators of locust occurrence and an essential indicator for damage assessment. Normalized Difference Vegetation Index (NDVI) is the most widely used vegetation index, given its sensitivity to vegetation growth, and its reflection of the luxuriance in vegetation. Numerous experimental results have proved the effectiveness of environmental predictors such as NDVI or soil moisture in an effort to identify favorable breeding areas based on machine learning methods. The aforementioned studies used isolated insect spots as targets, as locusts are easier to track (given their limited mobility within a short period of time). Hielkema *et al.* [7] built a desert locust density monitoring system based on NDVI calculated from NOAA/AVHRR satellite. Bryceson and Kim [8] found that reliable estimations of locust density can be obtained when desert locust monitoring is supported by the ground truth data. In the 1990s, Voss and Dreiser used multisource remote sensing data [mainly Landsat Thematic Mapper (TM)] to analyze the habitable factors of desert locusts in the Red Sea region of Sudan, aiming to find spawning places and potential vegetation coverage that are favored by locusts [9]. In addition, some studies used NOAA/AVHRR data, combined with meteorological information, to locate sites where desert locusts are prone to outbreak. The FAO has released "SWARMS" [10], [11], the first desert locust early warning and control system, which monitors the habitat information via real-time remote sensing data, and issues early warning for relevant countries and regions.

According to the above literatures, there are several problems in the research of locust plagues. 1) Most of the previous study of locust plague were based on MODIS or Landsat time-series data [6], [12], the data may exist clouds over the study area, and other preprocessing stages will affect the results. 2) The research data are mainly multispectral remote sensing data and rarely involve hyperspectral image data, and the vegetation changes before and after the locust plague are not studied in terms of spectrum. 3) The linear analysis of NDVI index is often used in locust monitoring research based on time-series data, without the model for complex analysis.

In order to overcome above drawbacks, this article uses the MODIS products (MOD13A2 and MOD11A2) to get NDVI and land surface temperature (LST) of the study area and extract the derived indices to analyze the habitat factors of locusts. Then, based on the time-series indices obtained from MODIS product data, this article uses hidden Markov model (HMM) to explore the relationship between these indices and the severity of locust occurrence, and to monitor and predict the occurrence of locusts.

In recent years, the development of hyperspectral satellites potentially facilitates locust plague monitoring and prediction. Hyperspectral imagery contains both reflection and radiation information, which is described by tens to hundreds of narrow bands corresponding to different narrow wavelength [13]. Hyperspectral imagery plays important roles in many fields [14]–[16], such as agriculture and geological surveys, due to its abundant spectral information that benefits the precise identification of objects [17], [18]. Therefore, to better monitor the impact of locust plague on vegetation spectrum, the high-spectral resolution of hyperspectral data is used to reflect the fine changes of vegetation spectrum and support the prediction and evaluation of locust disaster.

HMM [19] is a classic machine learning model, which has been widely used in fields of time-series data mining [20]–[22]. The study in [23] used HMM to predict the development of cracks under the action of hydraulic fracturing and dam deformation with long-term time-series data. Huang *et al.* proposed a fault diagnosis of the urban rail transit motor drive system based on improved HMM [22]. Ullah *et al.* predicted the energy consumption of residential buildings based on HMM [24]. Xiong *et al.* analyzed the dynamic vehicle ownership through HMM supported by time-series observation data [25]. HMM is a stochastic process to generate the observation sequence based on the state of a latent and unobserved Markov process. In this article, we feed features extracted from time-series remote sensing images to HMM (as observation state).

So, as to have a more specific understanding of the impact of locust plague, we use 10-m spatial resolution hyperspectral image for a small area change detection. Because hyperspectral imagery contains both reflection and radiation information plays important roles in many fields, such as agriculture and geological surveys, due to its abundant spectral information that benefits the precise identification of objects. Recently, there are many multisource methods for change detection and image classification. Chen *et al.* [26] proposed a method to fuse multisource remote sensed data for improving land cover classification. Sun *et al.* [27] using multisource and multitemporal remote sensing data to improve the crop-type mapping in subtropical agriculture region. Zhao *et al.* [28] proposed the hierarchical random walk network (HRWN) for joint classification of hyperspectral imagery and LiDAR data and achieved good results. Seydi *et al.* [29] proposed an end-to-end multidimensional CNN framework for land cover/land use change detection in multisource remote sensing datasets.

Therefore, to better monitor the effect of locust plague on vegetation spectrum, the high spectral resolution of hyperspectral data is used to reflect the fine changes of vegetation spectrum and support the prediction and evaluation of locust disaster. In this study, the main contribution includes: 1) This study pioneering utilize HMM to predict the desert locust severity-based MODIS time-series features and which is importantly referred for the same kinds of research works; 2) This study uses Zhuhai-1 hyperspectral satellite (Orbita Hyperspectral Satellite, OHS) hyperspectral data for substudy area (northern Narok, Kenya) cropland change detection to quantitatively analyze the damages caused by the locust plague.

This study aims to use HMM to predict the desert locust severity in the croplands of the study area ranges from 30°E–90°E, 10°S–40°N (covering around 20 countries and regions) from April to July by using MODIS time-series (January–June 2020) data. Meanwhile, we use Zhuhai-1 hyperspectral satellite (Orbita

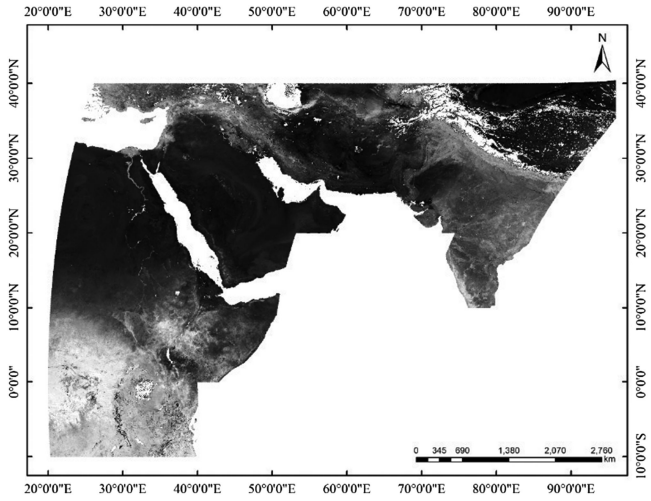

Fig. 1. Study area.

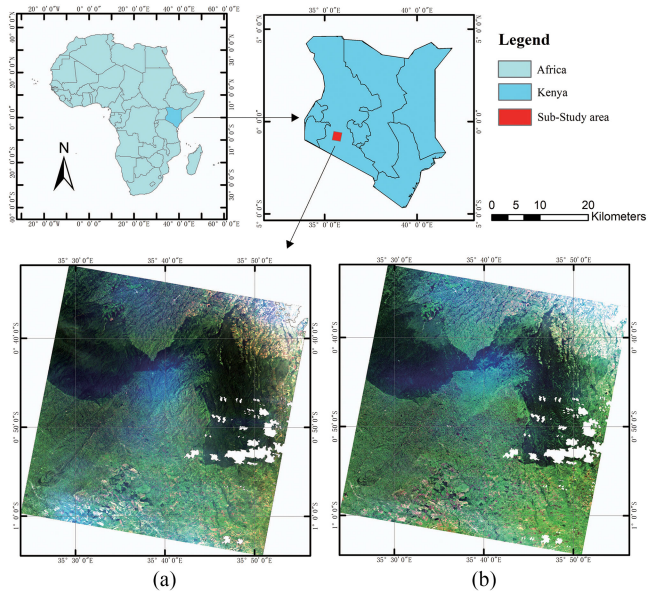

Fig. 2. Substudy area [(A) Febuary 23, 2020; (B) March 7, 2020].

Hyperspectral Satellite, OHS) hyperspectral data for substudy area (northern Narok, Kenya) cropland change detection to quantitatively analyze the damages caused by the locust plague.

II. Materials and Methodology

A. Study Area

The study area ranges from 30°E–90°E, 10°S–40°N as shown in Fig. 1 (covering around 20 countries and regions), characterized by four climate types: tropical savanna climate, tropical desert climate, tropical monsoon season, and temperate continental climate. The substudy area, covering 2556.3 km^2, is situated in northern Narok, Rift Valley county, Kenya (0°33'–1°01'S, 35°26'–35°53'E) (see Fig. 2). The climate across this region is a tropical savanna climate with an average altitude of 1.8 km. The coastal areas are hot and humid, and the plateau climate is mild. The annual average temperature is 22 °C–26 °C.

TABLE I
MODIS Single Period Strip Number Information

h20v05	h20v06	h20v07	h20v08	h20v09
h21v05	h21v06	h21v07	h21v08	h21v09
h22v05	h22v06	h22v07	h22v08	h23v05
h23v06	h24v05	h24v06	h25v05	h25v06
h25v07				

B. Satellite Data and Preprocessing

NDVI has been widely used to reflect the vegetation growth and vegetation cover land condition [30], [31]. Thus, we include NDVI in our input data to characterize the desert locust habitats. In addition, studies [32]–[34] have suggested the locusts are sensitive to surface temperature and dry humidity. Our input data also include the vegetation temperature condition index (VTCI) and temperature vegetation drought index (TVDI). We obtain the MODIS terrestrial standard product from the United States Geological Survey (USGS) website. [1] Images are organized in the TILE type, i.e., the earth is the reference system with SIN (ISIN, sinusoidal projection) as earth projection system. In this study, a total of 252 image scenes (from Jan. to Jun. 2020) are downloaded. Information regarding the strip number involved in a single period is shown in Table I. The splicing, projection, and format conversion are performed using MODIS Reprojection Tool (MRT) software.

1) Vegetation Cover: NDVI is a widely adopted indicator to reflect whether crops suffer from pests and diseases, which is calculated as formula1.

$$\mathrm{NDVI} = (\mathrm{NIR} - R) / (\mathrm{NIR} + R) \tag{1}$$

where NIR is the near infrared band, R is the read band. The leaves of healthy crops contain more chlorophyll, thus having a higher absorption rate in the red spectrum region and higher reflectance in the near-infrared spectrum region. If infested by locusts, the internal tissues of the leaves are destroyed, resulting in a decrease in absorption of the red spectrum region as well as the reflectivity in the near-infrared spectrum region. If infested by locusts, the internal tissues of the leaves are destroyed, resulting in a decrease in absorption of the red spectrum region as well as the reflectivity in the near-infrared spectrum region.

In research [35] targeted East Asian migratory locust and measured the spectral curve of *Phragmites australis* with different levels of damages in 2002 and analyzed the scope and degree of locust damage with MODIS data. The results showed that the reflectance of the damaged *Phragmites australis* increased in the red spectrum. The more serious the damage, the more significant the increase. The reflectance of the near-infrared spectrum was found significantly reduced. The changes of NDVI before and after the locust plague is essential for damage assessment, as the increase of the rapid decrease of NDVI generally indicates the damaged areas. Ma *et al.* proposed the disaster detection and prediction framework based on the characteristics of the biological development cycle of migratory locusts [36]. Their

[1] [Online]. Available: https://ladsweb.modaps.eosdis.nasa.gov/search

study used remote sensing data to obtain LST, soil moisture and leaf area index in the ovipositor, hatching, and nymph stages of locusts to analyze the outbreaks of East Asian migratory locust and predict the possibility of locust occurrence. Zha *et al.* [37] applied temporal filtering using MODIS time-series data to monitor the outbreak of locust plagues in eastern China. They identified the dynamic changes of NDVI in the locust habitats to reveal the damages locust plague on vegetation. Crooks *et al.* [38] used synthetic aperture radar (SAR) to monitor the soil moisture status areas with locust outbreaks. They studied the relationship between soil moisture and locust hatching degree by comparing soil moisture under vegetation cover and bare soil. Their further used high-precision soil moisture data to predict the possibility of locust hatching rate. Using MODIS data, Zhang *et al.* [39] proposed a prediction method that quantitatively retrieves habitat factors the locust need during the growing period. They evaluated the potential disaster risk for grassland locusts in Xinjiang, China, and largely improving locust disaster prevention and mitigation capabilities in Xinjiang region.

We use Terra-MODIS Version 6, a 16-day composite (MOD13A2) NDVI with a 1 km spatial resolution. As the temporal resolution is 16 days, two periods of NDVI products can be obtained every month. We use ArcGIS 10.3 software to obtain monthly NDVI data for the following change detection analysis.

2) LST: LST can provide vital and useful information on the thermal status of land surfaces and is widely implemented in formulating the energy and water budgets at the surface–atmosphere interface [40], [41]. LST plays an important role in the field of surface physical processes at regional and global scales and is widely used in many research fields such as climate [42], hydrology [43], soil moisture estimation [44], to list a few.

We use the MOD11A2 Version 6 product, which provides an average 8-day per-pixel LST and Emissivity (LST&E) in a 1 200 by 1 200 km grid. The value for each pixel in the MOD11A2 represents an average of all the corresponding MOD11A1 LST pixels collected within that 8-day period. Provided along with the daytime and nighttime surface temperature bands are associated with quality control assessments, observation times, view zenith angles, and clear-sky coverages along with bands 31 and 32 emissivities from land cover types. We derive LST in degrees Celsius by using the following:

$$L = 0.02 \times G - 273.15 \tag{2}$$

where G represents pixels' digital number and L is LST in Celsius (°C).

3) TVDI and VTCI: Wang *et al.* proposed a near-real-time drought monitoring method named VTCI and verified that VTCI is related to NDVI and LST changes [45]. However, these methods have certain deficiencies given the subjectivity of judging the degree of drought. [46] proposed TVDI, an index that describes the physiology of crops and wetness, to detect drought using a large amount of remote sensing data. The TVDI and VTCI serve as input factors of the locust occurrence probability prediction model (described in Section D.1) HMM) [38]. TVDI is calculated as:

$$\text{TVDI} = \frac{T_s - T_{s_{\min}}}{a + b \times \text{NDVI} - T_{s_{\min}}} \tag{3}$$

where $T_{s_{\min}}$ is the triangle of the minimum surface temperature recognized, which defines the wet edge, T_s is the surface temperature observed on a given pixel, and a and b are the parameters that define the dry edge data as a linear function $T_{s_{\max}} = a + b \times \text{NDVI}$, where $T_{s_{\max}}$ is a given NDVI observed for the highest surface temperature. The higher the TVDI value, the closer the pixel is to the dry edge, and the lower the soil moisture is. As the vegetation coverage increases, $T_{s_{\min}}$ generally increases. When the vegetation coverage is relatively small, the TVDI value increases [47]. Therefore, in practical applications, the shape of the wet edge should be determined according to the growth of the underlying surface vegetation.

VTCI is used for monitoring the degree of drought, especially the relative drought degree during a certain period of a specific year. VTCI not only considers the change of NDVI, but also considers the change of LST under the same NDVI value. VTCI can be calculated using the following formula:

$$\text{VTCI} = \frac{\text{LST}_{\text{NDVI}_{i,\max}} - \text{LST}_{\text{NDVI}_i}}{\text{LST}_{\text{NDVI}_{i,\max}} - \text{LST}_{\text{NDVI}_{i,\min}}} \tag{4}$$

where $\text{LST}_{\text{NDVI}_{i,\max}} = a + b \times \text{NDVI}_i$, $\text{LST}_{\text{NDVI}_{i,\max}} = a' + b' \times \text{NDVI}_i$. $\text{LST}_{\text{NDVI}_{i,\max}}$ and $\text{LST}_{\text{NDVI}_{i,\min}}$ represent the LST value when the NDVI_i achieves maximum and minimum, respectively. a, b, a', b' are undetermined coefficients. The smaller the value of VTCI, the more severe the relative drought. It is necessary to set the sampling interval in the calculation of the dry and wet edge Equations. The default sampling interval is set to 10, meaning that 1 sample is drawn from every 10 pixels for the calculation of the dry and wet edge Equations.

4) OHS Dataset: The Zhuhai-1 hyperspectral satellite was launched on April 26, 2018. The hyperspectral image has a spatial resolution of 10 m and a spectral resolution of 2.5 nm, ranging from 400 to 1 000 nm with 32 bands [48]. The information regarding the central wavelength is presented in Table II.

TABLE II
CENTER WAVELENGTH OF OHS HYPERSPECTRAL DATA

B	W	B	W	B	W	B	W
B01	466	B09	596	B17	716	B25	836
B02	480	B10	610	B18	730	B26	850
B03	500	B11	626	B19	746	B27	866
B04	520	B12	640	B20	760	B28	880
B05	536	B13	656	B21	776	B29	896
B06	550	B14	670	B22	790	B30	910
B07	566	B15	686	B23	806	B31	926
B08	580	B16	700	B24	820	B32	940

B denotes the bands number, W denotes the central wavelength (nm) of the band.

The OHS hyperspectral data are imported into ENVI 5.3 software for absolute calibration, atmospheric correction, and orthorectification [49]. The radiometric calibration is performed using

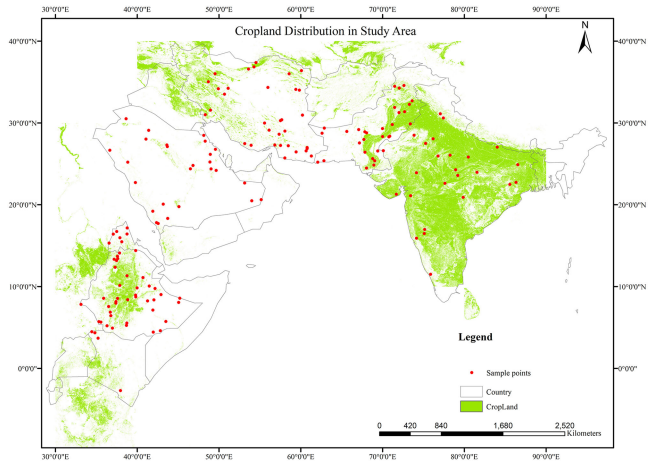

Fig. 3. Distribution of croplands and samples in the study area.

the following formula:

$$\text{Le} = \text{gain} \times \frac{\text{DN}}{\text{TDIStage}} + \text{offset} \tag{5}$$

where, Le is the apparent reflectance, $gain$ is the absolute radiometric calibration gain coefficient, *offset* is the absolute radiometric calibration offset coefficient, and $TDIStage$ is an integer series. We manually select 710 control points with total control error and single-point error both less than 0.5 pixels for image registration, making sure images are aligned well before the change detection.

C. Classification Map and FAO Bulletins as Reference

We use Finer Resolution Observation and Monitoring of Global Land Cover (FROM-GLC) (30 m) [50], FAO bulletin news and google earth data as the reference to select the sample points, making sure that the samples are located in cropland where invaded by locust plague. FROM-GLC is a global land cover product using Landsat TM and ETM+.[2] FROM-GLC includes a total of ten classes (i.e., cropland, forest, grassland, shrubland, wetland, water, tundra, impervious surface, bareland, and snow/ice) with an overall accuracy of over 71% [50]. Based on cropland distribution in the study area, we choose 164 samples for monitoring and predicting the locust severity from April to July, and FAO news bulletin as the ground truth to assess the accuracy of the predicted results.[3] The distribution of croplands and samples in the study area can be found in Fig. 3. The ground truth data selected from FAO bulletins are listed in the supplementary material.

D. Methodology

In this article, we utilize multisource of remote sensing data to predict and evaluate the locust severity and effects to the cropland. The MODIS series-time data is to extract the features (NDVI, TVDI) (day and night), LST (day and night), VTCI (day and night)) for HMM prediction in the whole study area. The

[2][Online]. Available: http://www.chinageoss.org

[3][Online]. Available: http://www.fao.org/ag/locusts/en/info/info/index.html

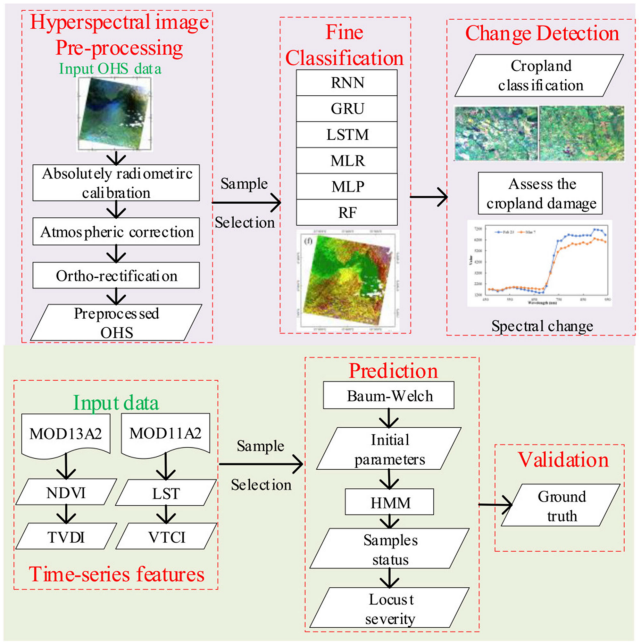

Fig. 4. Flowchart for predicting and assessing the locust severity of study area via multisource remote sensing data using HMM [vanilla recurrent neural network (RNN), RNN with gated recurrent unit (GRU), RNN with long short term memory (LSTM), multinomial logistic regression (MLR), multilayer perceptron (MLP), random forest (RF)].

hyperspectral OHS data is for fine classifying and evaluating the cropland changes. Because of the high spectral resolution of OHS, we can analyze the change of absorption spectrum peak in 450 and 680 nm of the vegetation, it is feasible to use hyperspectral image to damage crops caused by locusts. Fig. 4 presents the flowchart of our methodology, which includes details analytical processing steps and the data used. The methodology is divided into two parts: 1) the prediction of the severity of locusts in the large study area, 2) the cropland change detection of the substudy area. The specific procedures are as follows:

1) Prediction of the severity of locusts in the large study area: (A) The input data includes: time-series MOD13A2 and MOD11A2 data (from January to June), and the extracted features [NDVI, TVDI (day and night), LST (day and night), VTCI (day and night)]; (B) Selecting the cropland sample points in the study area referring to the Google earth data and FROM-GLC; (C) According to the reference data to classify the sample points locust severity levels; (D) Input the samples feature values into the HMM prediction Model; (E) The output is the status of sample points on the forecast date, the status is the severity level of locusts; (F) According to the reference data to evaluating the prediction results.

2) Change Detection of sub-study area: (A) The input data includes two original hyperspectral images (on February 23, 2020 and March 7, 2020); (B) Hyperspectral image preprocessing: (a) absolutely radiometric calibration; (b) atmospheric correction; (c) ortho-rectification; (C) Sample selecting; (D) Supervised classification; (E) The output is the classification results and accuracy.

1) HMM: HMM is a probability model describing the statistical characteristics of stochastic processes. HMM is composed

of state transition (Markov process) and observation sequence (a general stochastic process). HMM can be expressed using state transition matrix A, observation emission matrix B, and initial state probability π

$$\lambda = (A, B, \pi) \tag{6}$$

$$B = \left\{ b_j(y) | b_j(y) = P_{Y_t|X_t}\left(y|X_t = S_j\right), y \in \Omega_X, j \in \Omega_X \right\} \tag{7}$$

where, $A = [a_{ij}]_{N\times N}, i = 1, 2, \ldots, N$ denotes the probability of locust hazard level conversion, a_{ij} is the probability that the hidden state changes to S_j at $t+1$ when the hidden state is S_i at time t. Equation (7) describes the mapping, denoted as B, between the locust severity level X and the observation variable Y (remote sensing data). At t, Y_t represents the observation variable and X_t represents the corresponding hidden state. $b_j(y)$ is the conditional probability density of y when $X_t = S_j$. $\pi = \{\pi_i\}, i = 1, 2, \ldots, N$ denotes the probability distribution of hidden state at the initial time, i.e., $t = 0$. We use the Baum–Welch algorithm [51]to train the initial parameters from π, A, B. Baum–Welch algorithm identifies the extreme value by obtaining the partial derivative of the objective function constructed by the Lagrange multiplier method and establish the relationship between the parameters from the new model and the original model. Further, it substitutes the original parameters with the new parameters. The specific model parameter solving process is presented below. The initial parameters of the model can be represented as (6), and the observation vector is $y = (y_1, y_2, \ldots, y_t)$, denoted as $Y = y$. Other variables are defined as the following:

$$\zeta_k(i, j) = P\left(X_k = s_i, X_{k+1} = s_j | Y = y, \lambda\right) \tag{8}$$

$$\gamma_k(i) = P\left(X_k = s_i | Y = y\right) \tag{9}$$

where, $\zeta_k(i, j)$ denotes the possibility of hidden state changes from s_i to s_j when t changes from k to $k+1$. $\gamma_k(i)$ denotes the possibility of a hidden state s_j when $t = k (0 < k < T)$. According to the forward–backward algorithm and model definition, it can be derived

$$\begin{aligned}\gamma_k(i) &= P\left(X_k = s_i | Y = y, \lambda\right) \\ &= \frac{\alpha(i)\beta_k(i)}{\sum_{i=1}^{N}\sum_{i=1}^{N}\alpha_k(i)\alpha_{ij}b_i\left(y_{k+1}\right)\beta_{k+1}(j)}\end{aligned} \tag{10}$$

where $\alpha_k(i)$ and $\beta_k(i)$ are the forward and backward factors, respectively. Their calculations are as follows:

$$\hat{\pi} = \frac{p\left(Y = y, X_1 = s_i|\lambda\right)}{p\left(Y = y|\lambda\right)} = \gamma_1(i) \tag{11}$$

$$\begin{aligned}\hat{\alpha}_{ij} &= \frac{\sum_{k=1}^{T-1} p\left(Y = y, X_k = s_i, X_{k+1} = s_j|\lambda\right)}{\sum_{k=1}^{T-1} p\left(Y = y, X_k = s_j|\lambda\right)} \\ &= \frac{\sum_{k=1}^{T-1}\varsigma_k(i, j)}{\sum_{k=1}^{T-1}\gamma_k(i)}\end{aligned} \tag{12}$$

$$\begin{aligned}\hat{b}(l) &= \frac{\sum_{k=1}^{T} p\left(Y = y, X_k = s_j|\lambda\right)\delta\left(Y_k, \upsilon_i\right)}{\sum_{k=1}^{T} p\left(Y = y, X_k = s_j|\lambda\right)} \\ &= \frac{\sum_{k=1, Y_k=\upsilon_i}^{T-1}\gamma_k(j)}{\sum_{k=1}^{T}\gamma_k(i)}\end{aligned} \tag{13}$$

where, $\hat{\pi}$, $\hat{\alpha}_{i,j}$, and $\hat{b_j}$ are estimated values of initial state matrix, state transition probability matrix, and emission probability density, respectively. All initial model parameters are updated using (11)–(13), leading to the re-evaluated parameters $\hat{\lambda} = (\hat{A}, \hat{B}, \hat{\pi})$. Then, we compare $P_1 = P(Y = y|\hat{\lambda})$ and $P_2 = P(Y = y|\lambda)$. If $P_1 > P_2$, $\hat{\lambda}$ is more likely, compared to λ, to generate y. Thus, so λ is replaced by $\hat{\lambda}$. In this way, P_1 continues to increase until

$$\lambda^* = \max_{\lambda_i} P\left(Y = y|\lambda_i\right) \tag{14}$$

In this study, we select 164 sample points in cropland, according to FROM-GLC and FAO news of locust severity. Based on the FAO news, we divide the severity of locust plague into three levels: 1) calm, 2) serious, and 3) dangerous. Seven features (i.e., NDVI, LST_{day}, $\text{LST}_{\text{night}}$, TVDI_{day}, $\text{TVDI}_{\text{night}}$, VTCI_{day}, and $\text{VTCI}_{\text{night}}$) are extracted from MODIS time-series data and fed into the Baum–Welch algorithm to obtain model parameters. The trained parameters and time-series features are further input into the HMM model to predict the severity of the locust plague of sample points.

2) Extracting of Land Cover From OHS Data: a) Sample Selection: We take sentinel-2 image and FROM-GLC as the references and select the samples by visual interpretation. First, the land cover types in the substudy area are divided into vegetation areas and nonvegetation areas based on the visual interpretation from Google Earth. Second, the vegetation areas are divided into croplands and woodlands. Because we intend to analyze the change of cropland density, so according to the coverage degree, the croplands are further divided into high-density, medium-density, and low-density croplands. The woodlands are divided into high-density woodland, low-density woodland (as shown in Fig. 5). The samples number of different classes are shown in Table III.

b) Classification methods: To obtain classification results with better accuracy, the change detection of croplands in the substudy area is conducted based on OHS hyperspectral imagery via six classification methods: RF, MLR, MLP, vanilla RNN, RNN with GRU, RNN with LSTM.

TABLE III
NUMBER OF TRAINING, VALIDATION, AND TESTING SAMPLES USED IN SUBSTUDY AREA

Class	Training	Validation	Testing
Low-density Cropland	141,995	30,427	30,428
Non-vegetation	141,995	30,427	30,428
Low-density Woodland	141,995	30,427	30,428
High-density Woodland	141,995	30,427	30,428
Medium-density Cropland	141,995	30,427	30,428
High-density Cropland	141,995	30,427	30,428
Total	851,970	182,562	182,568

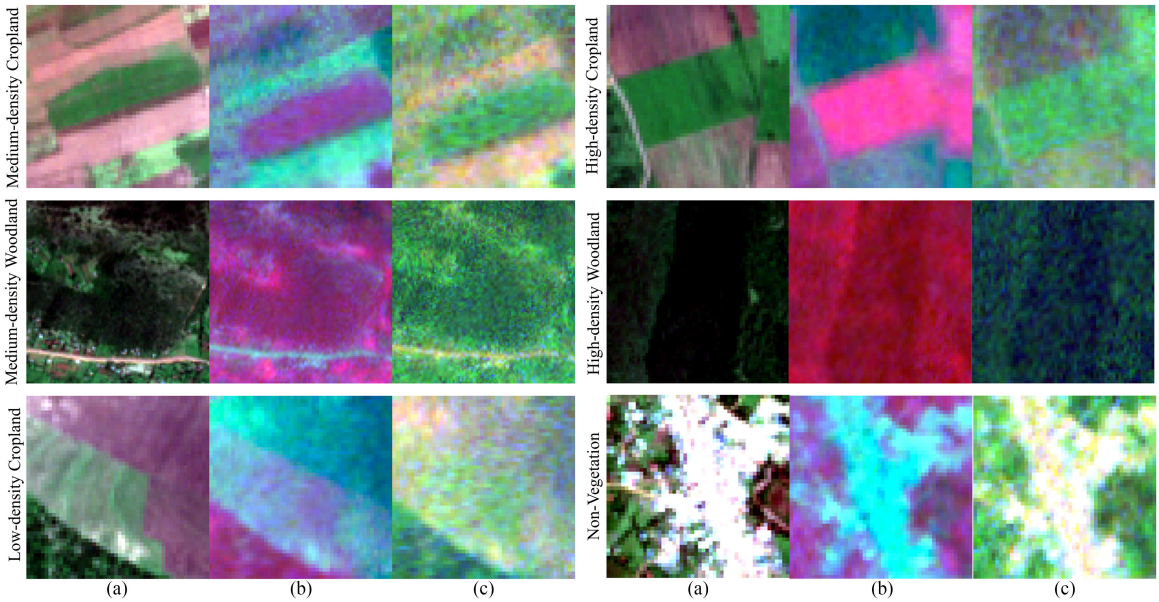

Fig. 5. Images of selected Medium-density cropland, Medium-density woodland, High-density cropland, High-density woodland, Low-density cropland, and nonvegetation, (a) (b) (c) is the image from sentinel-2, OHS false color, OHS true color, respectively.

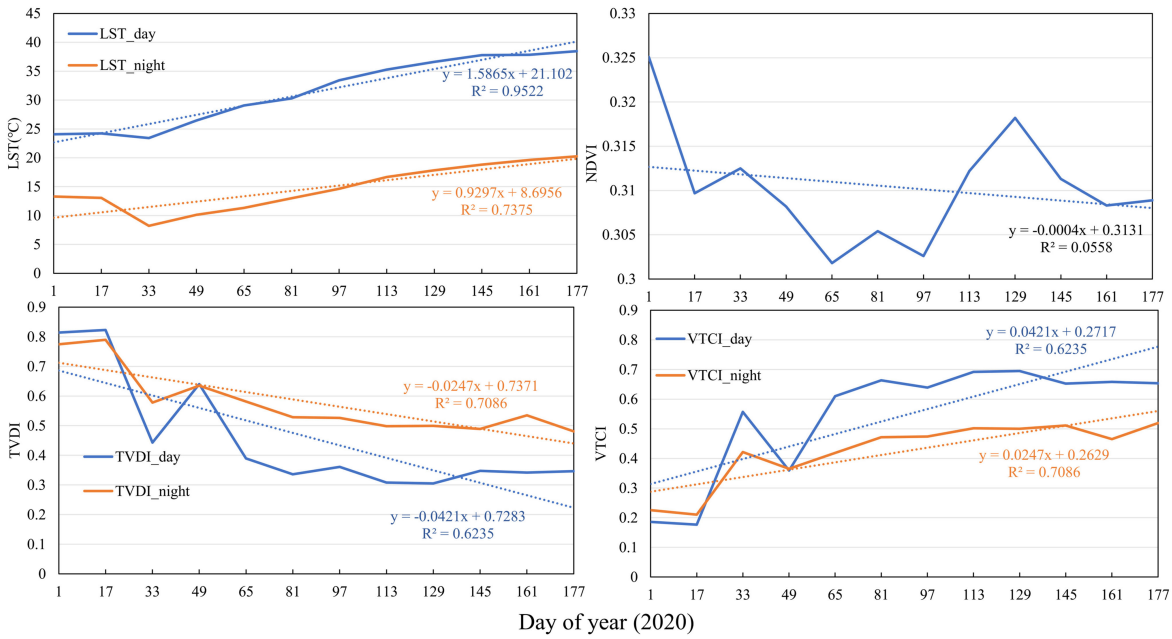

Fig. 6. Features moving average time-series in the study area.

III. Results and Analysis

A. Time-Series Features Dynamics in the Study Area

In this section, the times-series features of the study area are analyzed, namely NDVI, LST, TVDI, and VTCI. Fig. 6 shows the features moving average from day 1 to day 177, 2020 in the study area. R^2 is the correlation coefficient, indicating the change degree of the common trend of the two variables. R^2 denotes the coefficient of determination, which refers to the percentage of the change of one variable by the other variables to explain. It can be seen from Fig. 5 NDVI curve that the average value of NDVI continued to decrease from day 1 to day 97, and rapidly increased to the highest value from day 97 to day 129, and then gradually fell back again. The trendline also shows the declined of NDVI. As for LST, it is obviously that the temperature is increase while the season is from winter to summer. From Fig. 6, it can be seen that, from day 1 to day 177, TVDI declines and VTCI ascend, this is because the VTCI indicates the drought of the study area, and TVDI indicates the soil moisture. The feature curves indicates the climate is warming, and humid. The frequency of locust outbreak increases and at temperatures around 40 °C and a relative

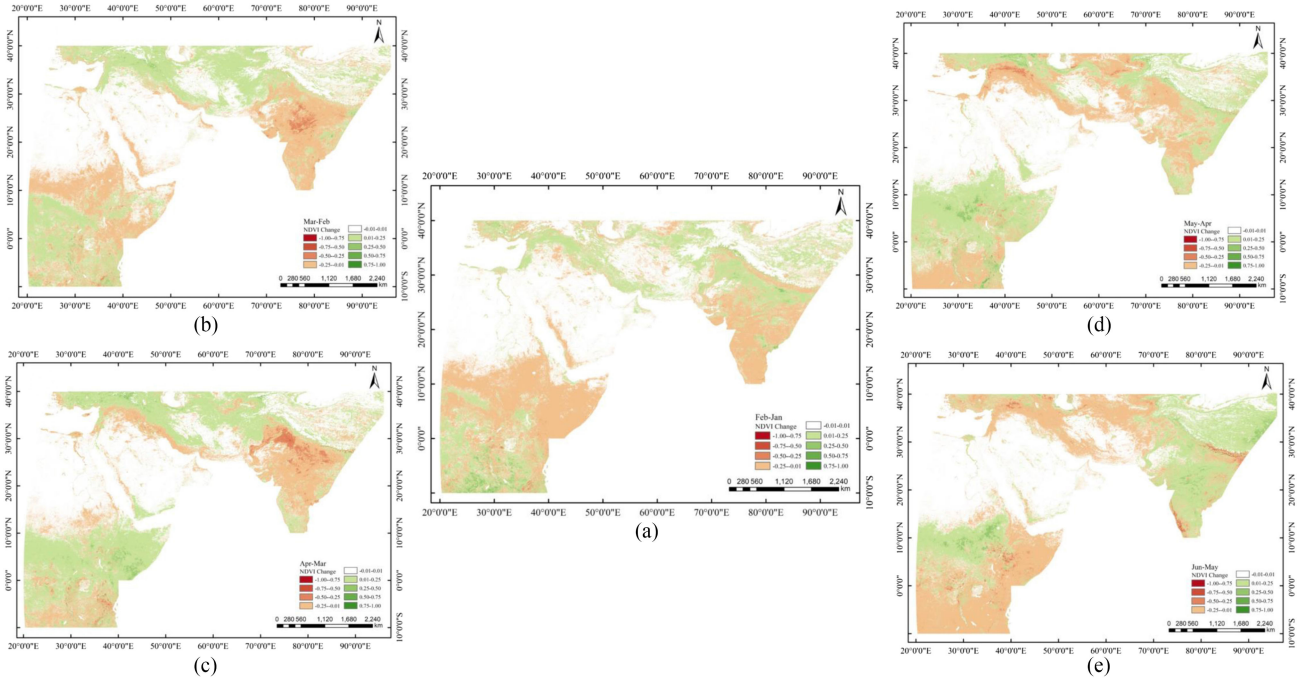

Fig. 7. NDVI changes from January to June 2020 ((a) February–January (b) March–February (c) April–March (d) May–April (e) June–May).

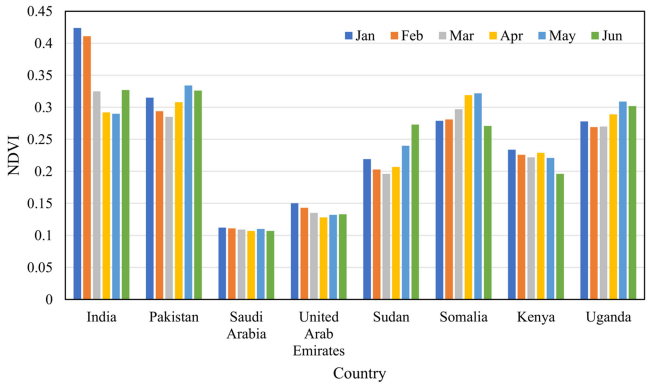

Fig. 8. The average value of NDVI in selected countries from January to June 2020.

humidity of 60%–70%, the locusts migrate and invade new land [52], [53].

The monthly variation of NDVI is considerably different from that of local growth. Season and vegetation distribution are closely related. NDVI changes range [-1, 1], where [-1, 0] represents the decrease in NDVI in two consecutive months, [0, 1] represents the increase in NDVI in two consecutive months. In ArcGIS, the division interval is 0.25 for hierarchical display, and the specific changes are shown in Fig. 7.

NDVI within the Horn of Africa has experienced a trend of "decreasing, increasing, and decreasing" from January to June 2020. The monthly change trends of NDVI in other countries within the study area are presented in Fig. 8. We notice that the NDVI of Sudan has the same trend as India, and the NDVI of very few countries such as Kenya has shown a general decreasing trend. NDVI in most countries is at a high level in May. Based on the analysis in Fig. 5, vegetation growth gradually appears in the northeast region and then spreads to the southwest region. This cycle occurs unevenly throughout the region. As the study area include many cross-climatic zones, the locusts are expected to migrate when drought occurs in some countries because they mainly feed on green plants [11]. According to the Pakistan National Locust Control Center, [4] surveillance and control operations were well underway in all the locust-affected provinces in Pakistan, involving partner organizations and FAO support from January to June 2020. Out of a total area of 437 900 km^2, 161 720 km^2 were declared as susceptible to locust attacks. As of April 26, 2020, overall 124 299 km^2 area had been surveyed in vulnerable areas, and 8 843 km^2 have been properly treated. Thanks to the treatment, the NDVI in Pakistan gradually increased.

Fig. 9 is the average of NDVI in Uganda, India, Kenya, Sudan. and Somalia from January to June 2018 to 2020. The NDVI growth trends of Uganda, Kenya, Sudan, and Somalia in 2020 are declined in various degree than 2019 and 2018. The NDVI of 2018, 2019, and 2020 in India are all decline, but in 2020, it declined most. In conclusion, comparing NDVI of the countries in 2020, 2018, and 2019, the decline in 2020 is obvious.

B. Locust Risk Degree Prediction in Study Area

The features extracted from MODIS products are from day 1 to day 177, 2020. We used the features from day 1 to day 81 to predict the sample points status on day 97; the features from day 17 to day 97 to predict the sample points status on day 113,

[4][Online]. Available: https://www.nlcc.gov.pk

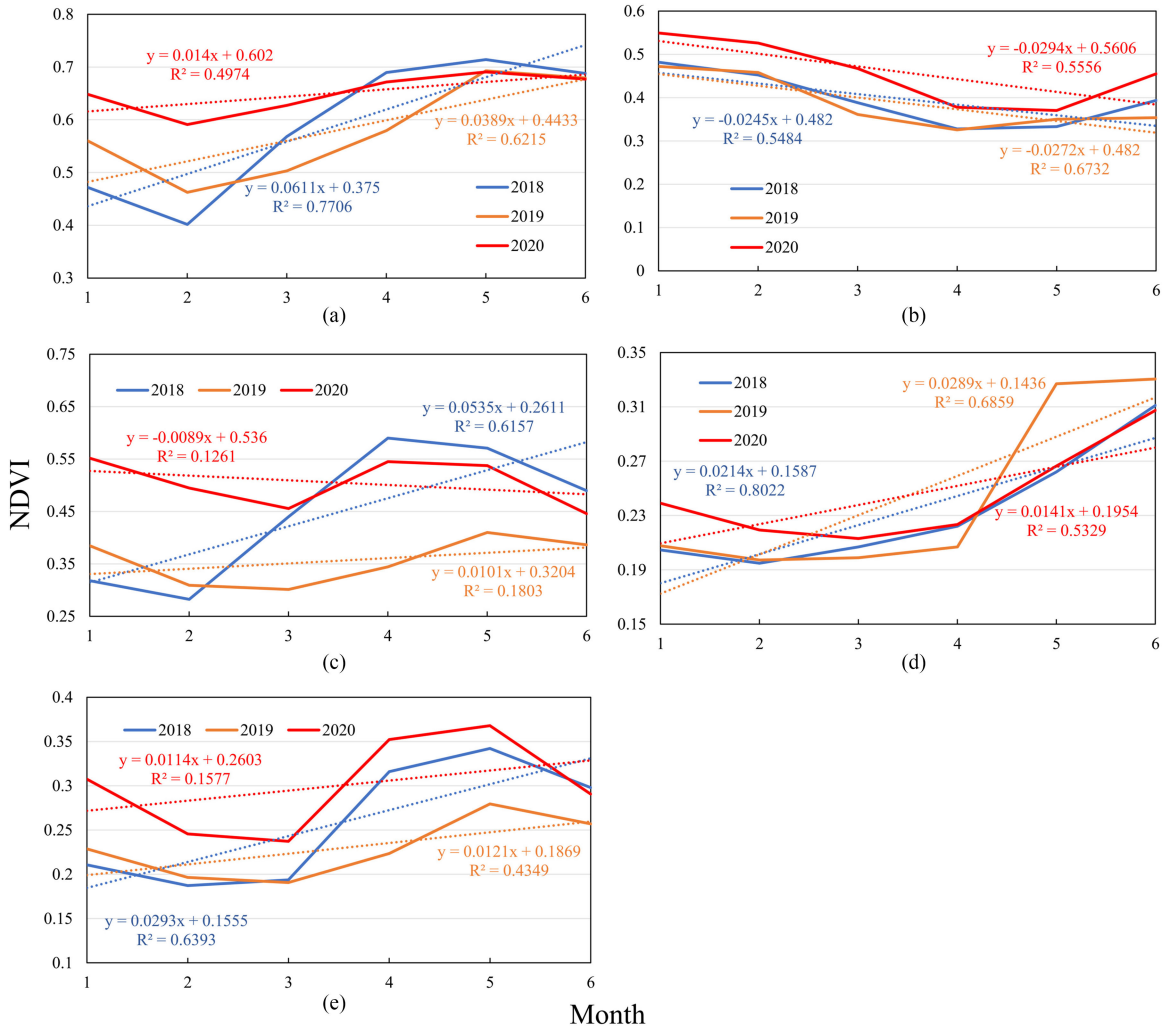

Fig. 9. The average value of NDVI in (a) Uganda, (b) India, (c) Kenya, (d) Sudan, and (e) Somalia from January to June 2018 to 2020.

and so on to day 177. The total predicted results (locust severity status of sample points) on day 97, 113, 129, 145, 161, and 177 are evaluated by comparing the predicted results with the actual values determined by the FAO news. All 164 samples were used for prediction and evaluation.

In order to illustrate the performance of HMM in predicting the damage degree of locusts, we use autoregressive integrated moving average (ARIMA) model as a comparison algorithm. ARIMA model is a differential integrated moving average autoregressive model, which is one of the most commonly used models for nonstationary time series prediction [54]. The OA and Kappa of the six groups of data using the same sample input data are lower than that of HMM model, so HMM is more suitable for prediction in this study area. HMM model is a stochastic process, which describes the hidden state and the observed state of a time series. HMM model can be used to model the evolution sequence of locust damage level, because the transfer of locust damage state in a large area is a Markov process, and the state of the next moment is only determined by this moment, and changes randomly with time.

TABLE IV
COMPARISON OF HMM AND ARIMA PREDICTION ACCURACY

Data of the year	HMM OA	HMM Kappa	ARIMA OA	ARIMA Kappa
97	**78.0488**	**0.664182**	62.8049	0.449888
113	**70.1220**	**0.548194**	54.8780	0.329240
129	**70.7317**	**0.563621**	57.9268	0.393095
145	**73.7805**	**0.594846**	60.3659	0.375818
161	**75.0000**	**0.617866**	62.1951	0.406614
177	**72.5610**	**0.563275**	59.1463	0.371517

We divide the locust damage severity into three levels: calm, serious, and dangerous, following the definition from FAO's new bulletin. From Table IV, it can be concluded that the OA in April (day 97), May (day 129), June (day 145), July (day 172) are 0.78, 0.71, 0.74, and 0.72, respectively. The corresponding confusion matrices are shown in Tables V– VIII.

From Fig. 10, we observe that in April, the locust plague in the horn of East Africa was still severe, especially in Ethiopia with the existence of croplands; locusts were distributed along the coast of the Red Sea and the Persian Gulf; the situation of locusts

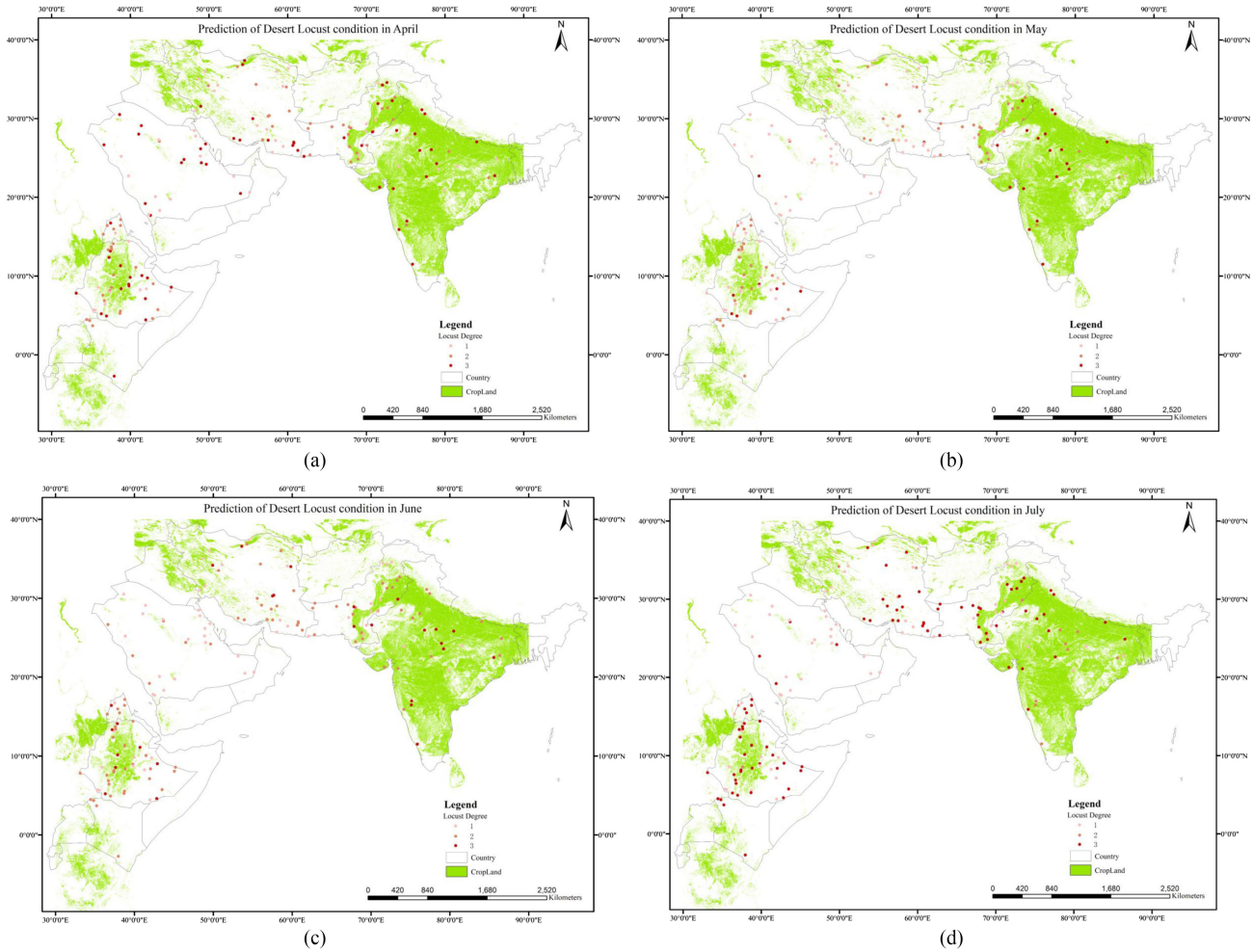

Fig. 10. HMM predicted locust plague severity in April to July 2020 ((a) April, (b) May, (c) June, (d) July).

TABLE V
CONFUSION MATRIX BETWEEN PREDICTED AND GROUND TRUTH LOCUST DAMAGE LEVELS IN APR

		HMM Prediction		
		Calm	Serious	Dangerous
Ground truth	Calm	31	0	4
	Serious	12	42	5
	Dangerous	3	12	55

TABLE VI
CONFUSION MATRIX BETWEEN PREDICTED GROUND TRUTH LOCUST DAMAGE LEVELS IN MAY

		HMM Prediction		
		Calm	Serious	Dangerous
Ground truth	Calm	35	2	6
	Serious	10	47	6
	Dangerous	9	15	34

TABLE VII
CONFUSION MATRIX BETWEEN PREDICTED GROUND TRUTH LOCUST DAMAGE LEVELS IN JUN

		HMM Prediction		
		Calm	Serious	Dangerous
Ground truth	Calm	60	2	2
	Serious	10	44	6
	Dangerous	9	13	18

TABLE VIII
CONFUSION MATRIX BETWEEN PREDICTED AND GROUND TRUTH LOCUST DAMAGE LEVELS IN JUL

		HMM Prediction		
		Calm	Serious	Dangerous
Ground truth	Calm	55	27	0
	Serious	0	45	8
	Dangerous	0	9	19

in southern Iran in Western Asia was severe, and the border between Pakistan and India was also invaded by locusts. At this time, most sample sites present severe locust plague. In May, the vegetation gradually entered a period of vigorous growth, and locusts were laying eggs, breeding, and growing. The locust plague condition in some sites changed to calm, except India and Pakistan, where the situation worsened.

Due to the frequent rainfall, a preferred condition for locusts to reproduce, in some areas, the severity of locust plague in many sites turned to a severe situation; locust plague in the corner of

TABLE IX
ACCURACY OF THE CLASSIFICATION RESULTS FROM OHS IMAGES ON FEBRUARY 23, 2020

Class	RNN	GRU	LSTM	MLR	MLP	RF
Low-density cropland	83.3541	94.1468	94.8074	79.1409	91.0280	**96.9239**
non vegetation	94.4360	92.3360	93.9464	71.2173	83.4593	**97.0783**
Low-density woodland	99.9836	99.9770	99.9638	99.9803	99.8784	**99.9901**
High-density woodland	92.8717	84.0706	87.3965	82.4044	67.4905	**95.7638**
Medium-density cropland	88.1951	94.8271	95.5929	81.7635	91.4980	**96.8647**
High-density cropland	96.2863	**98.7676**	98.0906	94.8140	94.3276	98.0906
OA	92.5211	94.0209	94.9663	84.8867	87.9470	**97.4519**
Kappa	0.910254	0.928250	0.939595	0.818641	0.855363	**0.969423**

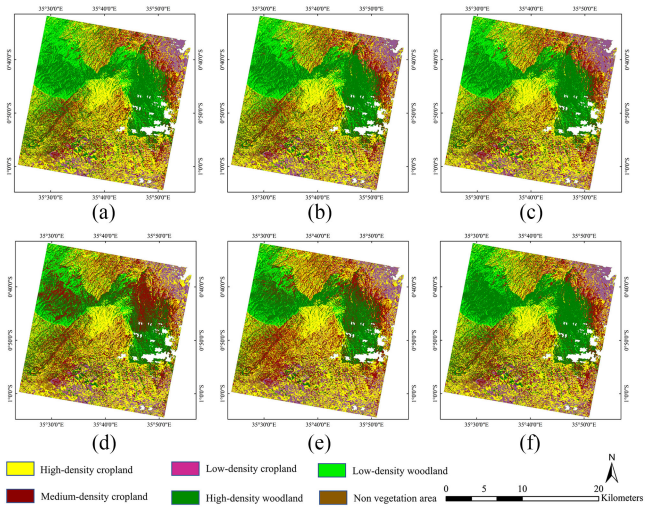

Fig. 11. Land cover types of OHS image on February 23, 2020 [(a) RNN, (b) GRU, (c) LSTM, (d) MLR, (e) MLP, (f) RF].

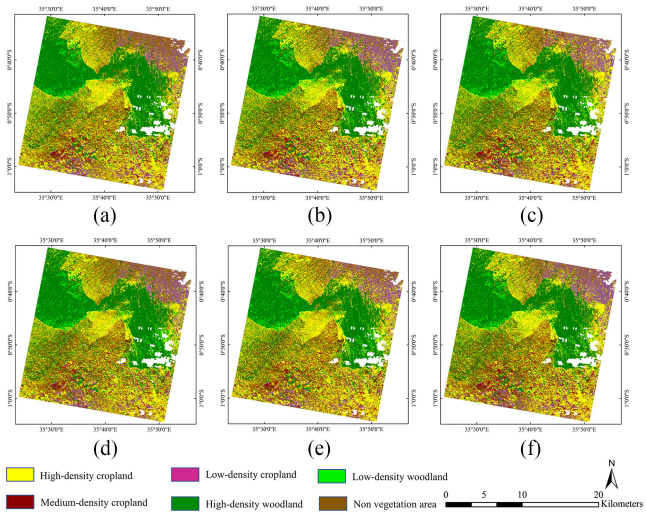

Fig. 12. Land cover types of OHS image on March 7, 2020 [(a) RNN, (b) GRU, (c) LSTM, (d) MLR, (e) MLP, (f) RF] .

East Africa gradually worsened, which was consistent with the NDVI trend in Fig. 7. The severe locust plague, coupled with the fact that India and Pakistan own a massive size of cultivated lands, posed a great threat to food security.

C. Substudy Area Vegetation Change Detection Based on OHS

1) Land Cover Classification Results: The extracted land covers of the substudy area on February 23 and March 7, 2020 based on six different classification methods (RNN, GRU, LSTM, MLR, MLP, RF) are shown in Figs. 11 and 12. The accuracy of the classification results is shown in Tables IX and X.

Tables IX and X show that RF has the highest overall classification accuracy, MLR and MLP have the lower accuracy. We can conclude from Tables IX and X that all the classification methods based on machine learning achieve better accuracy of land cover classification, with RF having the best performance. Therefore, we use the land cover classification results from RF to assess the locust damage.

To acquire a better knowledge of the land cover classification, we select subregions and superimpose the classification results on the OHS true-color image. It can be seen from Fig. 13(a) and (b) that the RF method is able to maintain the boundaries of land cover types, presenting great difference among croplands with different density, which can be used for subsequent crop area extraction and change detection.

The classification results show that the total area of croplands is 1 506 km^2. Croplands with high, medium, and low density in the study area on February 23 are 884 km^2, 421 km^2, and 201 km^2 in size, respectively. On March 7, the total area of croplands is 1 488 km^2, and croplands with high, medium, and low density are about 834 406, and 248 km^2, respectively. The locust plague led to decreases in croplands with high and medium density by 50 and 15 km^2, respective, around 4.43% of the substudy area. The results show that desert locusts have caused considerable damages to croplands, posing a great threat to food security in Kenya.

2) Change Detection Based on OHS: Fig. 14 shows the distribution of areas with decreased NDVI. Fig. 15 shows the cropland change distribution.

Comparing the damaged area (NDVI-reduced area) of the two images, we observe that, before the disaster, the reflectance of the crop was lower in the visible spectrum region. We find a green peak near 550 nm (B6), a red valley near 670 nm (B14), a near-infrared reflection peak near 820 nm (B24).

After the disaster, characteristics of green peak and red valley are weakened, indicating that the chlorophyll carriers (leaves, seedling ears, etc.) that can absorb or reflect red and green light are reduced. The reflectance changes greatly before and after the locust plague in the near-infrared region, also verifying that the

TABLE X
ACCURACY OF THE CLASSIFICATION RESULTS FROM OHS IMAGES ON MARCH 7, 2020

Class	RNN	GRU	LSTM	MLR	MLP	RF
Low-density cropland	94.2869	98.1026	95.7048	93.3069	95.3294	**97.2060**
non vegetation	95.9758	92.3061	90.2419	89.0534	90.2210	**96.6847**
Low-density woodland	93.3695	96.1635	90.3044	92.7648	91.8265	**96.6013**
High-density woodland	**98.0400**	96.0384	92.5354	93.4112	92.8482	94.9750
Medium-density cropland	95.0584	98.8741	98.1860	98.1860	97.4354	**99.1451**
High-density cropland	92.3269	91.6806	**93.2027**	91.5972	87.2811	92.2018
OA	94.8429	95.5275	93.3625	93.0532	92.4903	**96.1357**
Kappa	0.938115	0.946330	0.920350	0.916639	0.909883	**0.953628**

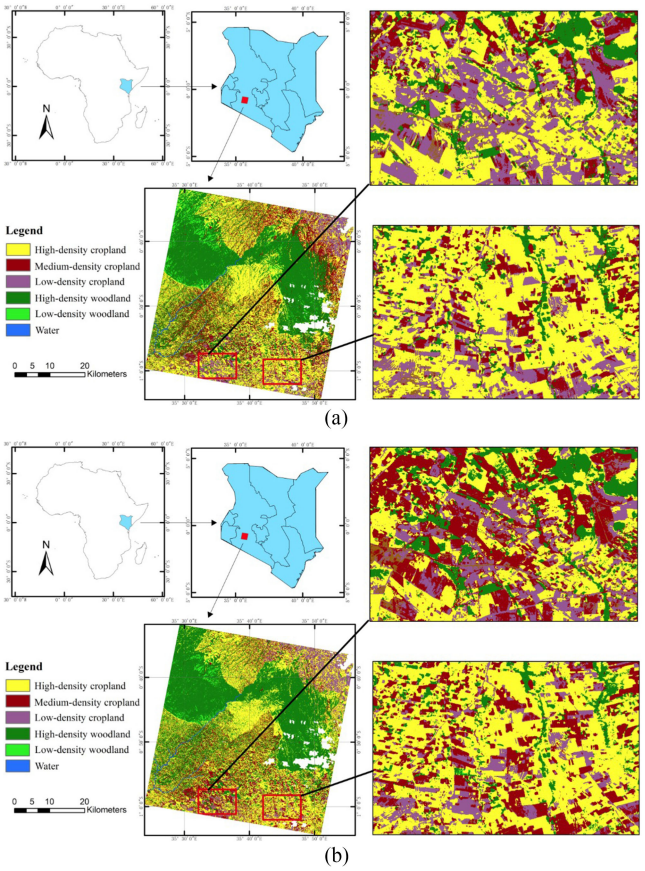

Fig. 13. Land cover classification results of RF from OHS images,(a) Classification result of February 23, 2020; (b) Classification result of March 7, 2020.

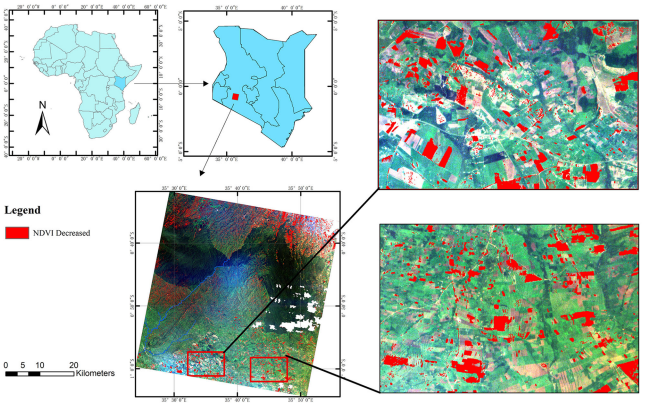

Fig. 14. Distribution of areas with decreased NDVI.

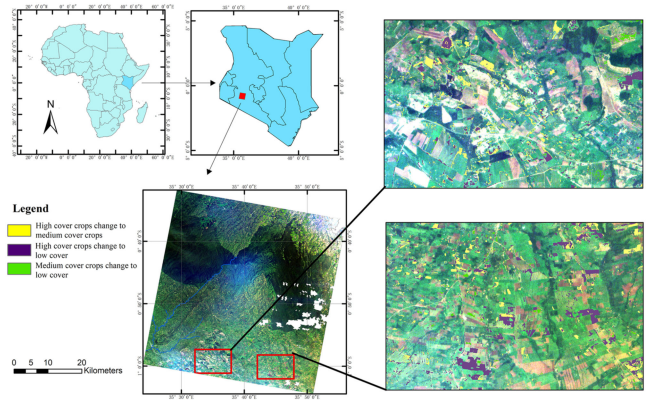

Fig. 15. Results of OHS classification in February 23 and March 7, 2020.

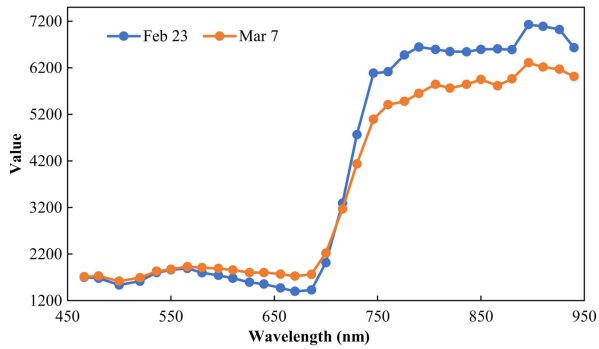

Fig. 16. Average spectra curves of croplands before and after locust plague.

crop canopy structure in these areas is damaged by locusts, as near-infrared reflectance is largely determined by the vegetation canopy structure. The results suggest that OHS hyperspectral data can accurately identify the changes in the spectral curves of croplands before and after the locust plague, facilitate the difference between healthy and affected crops, and providing essential knowledge to monitor the occurrence and the degree of a locust plague.

IV. CONCLUSION

The outbreak of the locust plague has caused severe damage to parts of Africa–Asia, resulting in crop reduction and serious

damage to forestry and grassland natural resources. The development of remote sensing technology facilitates large-scale, real-time monitoring of the occurrence of locust plagues and comprehensive damage assessment. We believe the locust plague can be observed using a corresponding vector sequence (such as the decrease of vegetation cover, the suitable temperature, and humidity of locusts, etc.). In this study, satellite time-series imagery is taken as observation data. Each observation vector is generated by a state sequence with the corresponding probability density distribution (locust severity). We input time-series NDVI, LST, TVDI and VTCI indices extracted from remote sensing data to predict the locust plague severity via HMM, a classic machine learning model that has been widely applied in the fields of time-series data mining. The accuracy of predicted results accuracy in April, May, June, July reached 0.78, 0.71, 0.74, and 0.72, respectively, indicating the effectiveness of the prediction method.

The change detection in substudy areas based on hyperspectral images reveals the quantitative impact of locust plague on crops, evidenced by the considerable decrease in croplands. The remote sensing time-series data provide reliable and rich information for large-scale locust plague monitoring and predicting. This study obtains fine-grained change detection of croplands taking advantage of the abundant spectral information of ground features provided by hyperspectral images, improving the accuracy of locust damage assessment. In future research, we consider incorporating more variables (e.g., soil moisture, climate, and hydrological factors) as the input observations for HMM to predict the locust severity.

ACKNOWLEDGMENT

The authors would like to thanks editors as well as the anonymous reviewers for their valuable suggestions and comments that helped us improve this paper significantly.

REFERENCES

[1] T. Woldai, "The status of earth observation (EO) & geo-information sciences in Africa - Trends and challenges," *Geo-Spatial Inf. Sci.*, vol. 23, no. 6, pp. 1–17, 2020.

[2] Z. Shao, N. S. Sumari, A. Portnov *et al.*, "Urban sprawl and its impact on sustainable urban development: a combination of remote sensing and social media data [J]," *Geo-Spatial Inf. Sci.*, vol. 24, no. 2, pp. 241–255, 2021.

[3] D. Li, Z. Shao, and R. Zhang, "Advances of geo-spatial intelligence at liesmars," *Geo-Spatial Inf. Sci.*, vol. 23, no. 6, pp. 1–12, 2020.

[4] R. Sivanpillai, A. V. Latchininsky, K. L. Driese, and V. E. Kambulin, "Mapping locust habitats in river Ili delta, Kazakhstan, using landsat imagery," *Agric. Ecosyst. Environ.*, vol. 117, no. 2/3, pp. 128–134, 2006.

[5] L. Mcculloch and D. M. Hunter, "Identification and monitoring of Australian plague locust habitats from Landsat," *Remote Sens. Environ.*, vol. 13, no. 2, pp. 95–102, 1983.

[6] D. Gómez, P. Salvador, J. Sanz, C. Casanova, D. Taratiel, and J. Casanova, "Desert locust detection using Earth observation satellite data in Mauritania," *J. Arid Environ*, vol. 164, pp. 29–37, 2019.

[7] J. Hielkema, J. Roffey, and C. Tucker, "Assessment of ecological conditions associated with the 1980/81 desert locust plague upsurge in West Africa using environmental satellite data," *Int. J. Remote Sens.*, vol. 7, no. 11, pp. 1609–1622, 1986.

[8] BRYCESON and P. Kim, "The use of landsat MSS data to determine the locust eggbeds of locust eggbeds in the Riverina region of New South Wales, Australia," *Int. J. Remote Sens.*, vol. 10, no. 11, pp. 1749–1762, 1989.

[9] F. Voss and U. Dreiser, "Mapping of desert locust habitats using remote sensing techniques[M]//New Strategies in locust control," *Birkhäuser Basel*, 1997, pp. 37–45.

[10] K. Cressman, "Swarms: A geographic information system for desert locust forecasting," in *New Strategies in Locust Control*. Berlin, Germany: Springer, 1997, pp. 27–35.

[11] F. Waldner, M. Ebbe, K. Cressman, and P. Defourny, "Operational monitoring of the desert locust habitat with Earth observation: An assessment," *ISPRS Int. J. Geo- Inf.*, vol. 4, no. 4, pp. 2379–2400, 2015.

[12] R. Cécile, W. FranOis, J. Damien, B. E. Mohamed, C. Keith, and D. Pierre, "A dynamic vegetation senescence indicator for near-real-time desert locust habitat monitoring with MODIS," *Remote Sens.*, vol. 7, no. 6, pp. 7545–7570, 2015.

[13] X. Feng, L. He, Q. Cheng, X. Long, and Y. Yuan, "Hyperspectral and multispectral remote sensing image fusion based on endmember spatial information," *Remote Sens.*, vol. 12, no. 6, 2020, Art. no. 1009.

[14] Z. Hou, W. Li, L. Li, R. Tao, and Q. Du, "Hyperspectral change detection based on multiple morphological profiles," in *IEEE Trans. Geosci. Remote Sens.*, 2021, to be published, doi: 10.1109/TGRS.2021.3090802.

[15] Z. Hou, W. Li, R. Tao, and Q. Du, "Three-order tucker decomposition and reconstruction detector for unsupervised hyperspectral change detection," in *IEEE J. Sel. Topics Appl. Earth Observ. Remote Sens.*, vol. 14, pp. 6194–6205, 2021, doi: 10.1109/JSTARS.2021.3088438.

[16] M. Hu, C. Wu, L. Zhang, and B. Du, "Hyperspectral anomaly change detection based on autoencoder," in *IEEE J. Sel. Topics Appl. Earth Observ. Remote Sens.*, vol. 14, pp. 3750–3762, 2021, doi: 10.1109/JSTARS.2021.3066508.

[17] X. Feng, L. He, Y. Zhang, and Y. Tang, "An optimization method for hyperspectral endmember extraction based on K-SVD," *Photogramm. Eng. Remote Sens.*, vol. 85, no. 12, pp. 879–887, 2019.

[18] F. Huang, Y. Yu, and T. Feng, "Hyperspectral remote sensing image change detection based on tensor and deep learning," *J. Vis. Commun. Image Representation*, vol. 58, pp. 233–244, 2019.

[19] L. E. Baum and J. A. Eagon, "An inequality with applications to statistical estimation for probabilistic functions of Markov processes and to a model for ecology," *Bull. Amer. Math. Stat*, vol. 37, no. 3, pp. 360–363, 1967.

[20] N. Asadi, A. Mirzaei, and E. Haghshenas, "Creating discriminative models for time series classification and clustering by HMM ensembles," *IEEE Trans. Cybern.*, vol. 46, no. 12, pp. 2899–2910, Dec. 2016.

[21] A. Ljolje, Levinson, and E. S., "Development of an acoustic-phonetic hidden Markov model for continuous speech recognition," *IEEE Trans. Signal Process.*, vol. 39, no. 1, pp. 29–39, Jan. 1991.

[22] H. Darong, K. Lanyan, C. Xiaoyan, Z. Ling, and M. Bo, "Fault diagnosis for the motor drive system of urban transit based on improved hidden Markov model," *Microelectron. Rel.*, vol. 82, pp. 179–189, 2018.

[23] D. H. Nguyen-Le, Q. B. Tao, V. H. Nguyen, M. Abdel-Wahab, and H. Nguyen-Xuan, "A data-driven approach based on long short-term memory and hidden Markov model for crack propagation prediction," *Eng. Fracture Mech.*, vol. 235, 2020, Art. no. 107085.

[24] U. Israr, A. Rashid, and K. Dohyeun, "A prediction mechanism of energy consumption in residential buildings using hidden Markov model," *Energies*, vol. 11, no. 2, 2018, Art. no. 358.

[25] C. Xiong, D. Yang, and L. Zhang, "A high-order hidden Markov model and its applications for dynamic car ownership analysis [J]," *Transp. Sci.*, vol. 52, no. 6, pp. 1365–1375, 2018.

[26] B. Chen, B. Huang, and B. Xu, "Multi-source remotely sensed data fusion for improving land cover classification," *ISPRS J. Photogramm. Remote Sens.*, vol. 124, pp. 27–39, 2017.

[27] C. Sun, Y. Bian, T. Zhou, and J. Pan, "Using of multi-source and multi-temporal remote sensing data improves crop-type mapping in the subtropical agriculture region," *Sensors*, vol. 19, no. 10, 2019, Art. no. 2401.

[28] X. Zhao *et al.*, "Joint classification of hyperspectral and Lidar data using hierarchical random walk and deep CNN architecture," *IEEE Trans. Geosci. Remote Sens.*, vol. 58, no. 10, pp. 7355–7370, Oct. 2020.

[29] S. T. Seydi, M. Hasanlou, and M. Amani, "A new end-to-end multi-dimensional CNN framework for land cover/land use change detection in multi-source remote sensing datasets," *Remote Sens.*, vol. 12, no. 12, 2020, Art. no. 2010.

[30] Z. Li, C. Xiaoling, C. Xiaobin, and H. A. Salim, "Spatial-temporal changes of NDVI and their relations with precipitation and temperature in Yangtze River Basin from 1981 to 2001," *Geo-spatial Inf. Sci.*, vol. 13, no. 3, pp. 186–190, 2010.

[31] B. Qiu, L. I. Weijiao, M. Zhong, Z. Tang, and C. Chen, "Spatiotemporal analysis of vegetation variability and its relationship with climate change in China," *Geo-spatial Inf. Sci.*, vol. 17, no. 3, pp. 170–180, 2014.

[32] N. Coggan, F. J. Clissold, and S. J. Simpson, "Locusts use dynamic thermoregulatory behaviour to optimize nutritional outcomes," *Proc. Roy. Soc. B, Biol. Sci.*, vol. 278, no. 1719, pp. 2745–2752, 2011.
[33] M. J. Escorihuela *et al.*, "SMOS based high resolution soil moisture estimates for desert locust preventive management," *Remote Sens. Appl., Soc. Environ.*, vol. 11, pp. 140–150, 2018.
[34] G. Yu, H. Shen, and J. Liu, "Impacts of climate change on historical locust outbreaks in China [J]," *J. Geophys. Res., Atmos.*, vol. 114, no. D18, 2009.
[35] J. I. Rong, B. Y. Xie, L. I. Dian-Mo, H. Yuan, and H. S. Yang, "Effects of reed population pattern on spatial distribution of Locusta migratoria manilensis in Nandagang wetland," *Chin. Bull. Entomol.*, 2007.
[36] M. A. Jianwen, H. Xiuzhen, H. A. Shibagan, W. Zhigang, Y. Shouxun, and D. Qin, "Remote sensing new model for monitoring the east asian migratory locust infections based on its breeding circle," *J. Remote Sens.*, vol. 8, no. 4, pp. 370–377, 2004.
[37] Y. Zha, J. Gao, S. Ni, and N. Shen, "Temporal filtering of successive modis data in monitoring a locust outbreak," *Int. J. Remote Sens.*, vol. 26, no. 24, pp. 5665–5674, 2005.
[38] W. T. Crooks and R. A. Cheke, "Soil moisture assessments for brown locust *Locustana pardalina* breeding potential using synthetic aperture radar," *J. Appl. Remote Sens.*, vol. 8, no. 1, 2014, Art. no. 084898.
[39] X. Zhang, J. Rao, and Y. Pan, "Progressive approach for risk prediction of rangeland locust hazard in Xinjiang based on remotely sensed data," *Nongye Gongcheng Xuebao/Trans. Chin. Soc. Agric. Eng.*, vol. 31, no. 11, pp. 202–208, 2015.
[40] M. C. Anderson, J. M. Norman, W. P. Kustas, R. Houborg, P. J. Starks, and N. Agam, "A thermal-based remote sensing technique for routine mapping of land-surface carbon, water and energy fluxes from field to regional scales," *Remote Sens. Environ.*, vol. 112, no. 12, pp. 4227–4241, 2008.
[41] A. Karnieli *et al.*, "Use of NDVI and land surface temperature for drought assessment: Merits and limitations," *J. Climate*, vol. 23, no. 3, pp. 618–633, 2010.
[42] J. Hansen, R. Ruedy, M. Sato, and K. Lo, "Global surface temperature change," *Rev. Geophys.*, vol. 48, 2010, Art. no. RG4004, doi: 10.1029/2010RG000345.
[43] W. T. Crow and E. F. Wood, "The assimilation of remotely sensed soil brightness temperature imagery into a land surface model using ensemble Kalman filtering: A case study based on estar measurements during SGP97," *Adv. Water Resour.*, vol. 26, no. 2, pp. 137–149, 2003.
[44] A. Amazirh *et al.*, "Retrieving surface soil moisture at high spatio-temporal resolution from a synergy between Sentinel-1 radar and Landsat thermal data: A study case over bare soil," *Remote Sens. Environ.*, vol. 211, pp. 321–337, 2018.
[45] M. Wang, S. Yang, G. Dong *et al.*, "Estimating soil water in northern China based on vegetation temperature condition index (VTCI) [J]," *Arid Land Geogr.*, 2012, p. 3.
[46] I. S. A., K. R. A., and J. A. B., "A simple interpretation of the surface temperature/vegetation index space for assessment of surface moisture status," *Remote Sens. Environ.*, vol. 79, no. 2/3, pp. 213–224, 2002.
[47] Q. Zhuang, S. Wu, X. Feng, and Y. Niu, "Analysis and prediction of vegetation dynamics under the background of climate change in Xinjiang, China," *PeerJ*, vol. 8, 2020, Art. no. e 8282.
[48] Y. Jiang, J. Wang, L. Zhang, G. Zhang, and J. Wu, "Geometric processing and accuracy verification of Zhuhai-1 hyperspectral satellites," *Remote Sens.*, vol. 11, no. 9, 2019, Art. no. 996.
[49] D. Fawcett, W. Verhoef, D. Schläpfer, F. D. Schneider, M. E. Schaepman, and A. Damm, "Advancing retrievals of surface reflectance and vegetation indices over forest ecosystems by combining imaging spectroscopy, digital object models, and 3D canopy modelling," *Remote Sens. Environ.*, vol. 204, pp. 583–595, 2018.
[50] P. Gong *et al.*, "Finer resolution observation and monitoring of global land cover: First mapping results with Landsat TM and ETM data," *Int. J. Remote Sens.*, vol. 34, no. 7, pp. 2607–2654, 2013.
[51] L. R. Welch, "Hidden Markov models and the Baum-Welch algorithm," *IEEE Inf. Theory Soc. Newslett.*, vol. 53, no. 2, pp. 194–211, Dec. 2003.
[52] S. Veran *et al.*, "Modeling spatiotemporal dynamics of outbreaking species: Influence of environment and migration in a locust," *Ecology*, vol. 96, no. 3, pp. 737–748, 2015.
[53] G. Hurst, "Meteorology and locust migrations," *Nature*, vol. 205, pp. 661–662, 1965.
[54] B. O. Elgabbanni, M. O. Khozium, and M. A. Ahmed, "Combination prediction model of traffic accident using rough set technology approach," *Int. J. Enhanced Res. Sci. Technol. Eng.*, vol. 3, no. 1, pp. 47–56, 2014.

Zhenfeng Shao received the bachelor's in surveying engineering and master's degrees in cartography and geographical information system from Wuhan Technical University of Surveying and Mapping, Wuhan, China, respectively, in 1998 and 2001, and the Ph.D. degree in photogrammetry and remote sensing from Wuhan University, Wuhan, China, in 2004.

He is currently a Professor in State Key Laboratory of Information Engineering in Surveying, Mapping, and Remote Sensing, Wuhan University, Wuhan, China. The specific research directions include high-resolution remote sensing image processing and analysis, key technologies and applications from digital cities to smart cities and sponge cities. His research interests include urban remote sensing applications.

Xiaoxiao Feng received the bachelor's degree in surveying and mapping from Southeast University, Nanjing, China, in 2014, and the master's degree in earth exploration and information technology from the China University of Geology, Wuhan, China, in 2017. She is currently working toward the Ph.D. degree with the State Key Laboratory of Information Engineering in Surveying, Mapping and Remote Sensing (LIESMARS), Wuhan University, Wuhan, China.

Her research interests include hyperspectral image processing and urban impervious surface extraction.

Linze Bai received the bachelor's degree in remote sensing science and technology from Wuhan University, Wuhan, China, in 2019. He is currently working toward the master's degree in photogrammetry and remote sensing with the State Key Laboratory of Surveying, Mapping, and Remote Sensing Information Engineering, Wuhan University, Wuhan, City.

His research interests include vegetation remote sensing and impervious surface extraction.

Haiming Jiao received the master's degree in surveying science and technology from Henan Polytechnic University, Jiaozuo, China, in 2019.

He is currently a RA Student with Wuhan University, Wuhan, China. His research interests include vegetation and ecological monitoring.

Ya Zhang received the master's degree in agricultural information engineering from Shihezi University, Xinjiang, China, in 2018. She is currently working toward the Ph.D. degree in photogrammetry and remote sensing with the State Key Laboratory of Information Engineering in Surveying, Mapping and Remote Sensing (LIESMARS), Wuhan University, Wuhan, China.

Her research interests include remote sensing of urban vegetation and ecological environment remote sensing.

Deren Li received the bachelor's and master's degrees from Wuhan University, Wuhan, China, and the Ph.D. degree from the Stuttgart University of Germany, Stuggart, in 1963, 1981, and 1985, respectively, all in photogrammetry and remote sensing.

He is currently a Professor with the State Key Laboratory of Information Engineering in Surveying, Mapping and Remote Sensing, Wuhan University, Wuhan, China.

Prof. Li was selected as a member of Chinese Academy of Sciences in 1991 and a member of Chinese Academy of Engineering in 1994. He was awarded the title of honorary doctor from ETH Zürich, Switzerland in 2008.

Haisheng Fan received the Ph.D. degrees in cartography and geographical information system from Peking University, Beijing, China, in 2001.

He is currently the Executive Vice President with the Guangdong Orbit Institute of Artificial Intelligence. From 2001 to 2008, he was the Chief Researcher with Basic Engineering Co., Ltd., Japan, mainly engaged in the design and development of satellite remote sensing application system, image processing algorithm, environmental change monitoring model, etc., as well as, from 2008 to 2011, he was the special Lecturer with Lizheng University, mainly engaged in the education of remote sensing image processing, geographic information system, computer network.

Xiao Huang received the bachelor's degree in remote sensing and information engineering from Wuhan University, Wuhan, China, in 2015, the master's degree in city planning and architecture from the Georgia Institute of Technology, Atlanta, GA, USA in 2016, and the Ph.D. degree in geography with the University of South Carolina, Columbia, SC, USA, in 2020.

He is currently an Assistant Professor with the Department of Geosciences, the University of Arkansas, Fayetteville, AR, USA. His research interests include remote sensing and GIS in natural hazards, data-driven visualization and advanced data fusion flood models, big social data mining, regional geospatial analysis, remote sensing, and GeoAI.

Yuqi Ding received the bachelor's and master's degrees in geographical information system from Wuhan University, Wuhan, China, in 2009 and 2013, respectively. He is currently working toward the Ph.D. degree in the Division of Computer Science and Engineering, Louisiana State University, Baton Rouge, Louisiana.

His research interests include computational photography, computer vision, and computer graphics.

Orhan Altan received the master's degrees in civil engineering from Istanbul Polytechnic University, Istanbul, Turkey, in 1970.

From 1972 to 1973, he studied at ETH Zurich Institute of Geodest and Photogrammetry. From 2000 to 2004, he was the Director of ISPRS. From 2004 to 2008, he was the Secretary General of ISPRS, from 2008 to 2012, the Chairman of ISPRS, and from 2012 to 2016, the first Vice Chairman of ISPRS.

Prof. Altan is currently the Honorary Member of ISPRS and Science Academy, an Honorary Fellow of Indian Society of Remote Sensing, and from 2011 to 2018, a member of Executive Council of International Council of Science.

Nayyer Saleem received the bachelor's degree in mathematics and physics from the University of the Punjab, Lahore, Pakistan, in 2005, and the master's degree in geo-informatics from the Faculty of Geo-Information Science and Earth Observation, University of Twente, Enschede, the Netherlands, in 2014. Since 2007, he has been working toward the Ph.D. degree in photogrammetry and remote sensing with LIESMARS, Wuhan University, Wuhan, China.

In 2007, he joined National Mapping Organization. He is currently working as Deputy Director with the Survey of Pakistan.